

pubs.acs.org/ac Article

A Synchrotron-Based Vacuum Ultraviolet Photoionization Mass Spectrometer-Coupled Microreactor To Probe Thermocatalysis

Dababrata Paul, ** Souvick Biswas, ** Nureshan Dias, Matthew T. Finn, Andrew S. Lipton, Albert Epshteyn, ** Musahid Ahmed, ** and Ralf I. Kaiser **

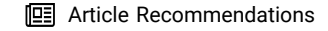


Cite This: Anal. Chem. 2025, 97, 22846–22857



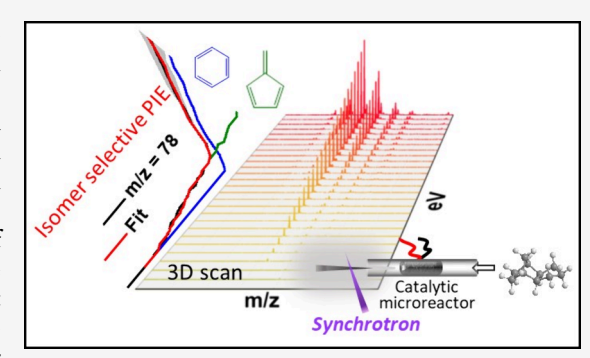
ACCESS

III Metrics & More



s Supporting Information

ABSTRACT: Vacuum ultraviolet photoionization (VUV-PI) mass spectrometry offers an isomer-selective and universal ionization with minimal fragmentation detection of organics in complex chemical systems such as pyrolysis and combustion. Here, we report a state-of-the-art experimental setup of a universal catalytic microreactor combined with a molecular beam to investigate the thermocatalytic oxidation of a heterogeneous system relevant for probing reactions at gas—solid interfaces. In strong contrast to traditional off-line analytical methods, this technique is capable of identifying and quantifying short-lived species (radicals) as well as stable products to decipher initial reaction steps via the detection of nascent products. The thermocatalytic oxidative degradation of exo-tetrahydro-dicyclopentadiene (JP-10), a high energy-density hydrocarbon fuel, over



solid titanium—aluminum—boron reactive mixed metal nanopowder (Ti-Al-B RMNP) is exploited to showcase potential applications. Overall, some 59 nascent gas-phase products are identified via photoionization efficiency (PIE) curves, including oxygenated species and hydrocarbons comprising closed-shell molecules and radicals. The critical temperature for complete oxidative decomposition of JP-10 was lowered by 450 K from 1400 K to 950 K, indicating an efficient thermocatalytic action of Ti-Al-B nanoparticles on JP-10. The enabling of a universal chemical microreactor along with VUV-PI mass spectrometry broadens the applicability of this technique to hydrocarbon fuel oxidation and pyrolysis characterization. This isomer-selective sensitive probing along with the detection of radical transients makes the aforementioned technique superior to other conventional analytical techniques such as microflow tube and pyrolysis-gas chromatography coupled with mass spectrometry for investigating similar pyrolysis reactions and comprehensive quantification.

■ INTRODUCTION

High-energy-density hydrocarbon fuels are crucial for enhanced performances of volume-limited air-breathing propulsion systems for greater flight range developed in sophisticated aircraft, racing and jet engines, and military vehicles. 1-5 Owing to the high thermal stability, however, the use of hydrocarbon fuels faces challenges such as incomplete combustion and long ignition delay. 6,7 Solid nanoadditives, including metallic nanoparticles such as aluminum (Al), boron (B), and cerium (Ce), have been previously reported as enhancing combustion efficiency.^{5,7–12} These types of additives can act in various ways such as nucleation sites during combustion, which can lead to rapid boiling of the fuel through heat transfer and consequent faster burning rates. However, the detailed chemistry that occurs during nanofuel burning is more diverse and cannot be captured at the mechanistic level by simply quantifying the combustion efficiency. For example, the use of aluminum nanoparticles (AINP) as an additive to high density hydrocarbon fuel exotetrahydrodicyclopentadiene (JP-10) generates gaseous aluminum monoxide (AlO) and hydroxyl (OH) radicals at the initial

stages of decomposition and oxidation process, serving as a precursor to JP-10 oxidation and thus controlling overall efficiency and performance. However, the information on the primary decomposition products of the hydrocarbon (JP-10) itself could not be identified in these experimental approaches. Hence, it is highly desirable to develop a novel analytical technique that can provide a comprehensive inventory and quantification of the nascent products, which will enable an improved understanding of the reaction mechanism for various complex processes occurring in the presence of such fuel additives.

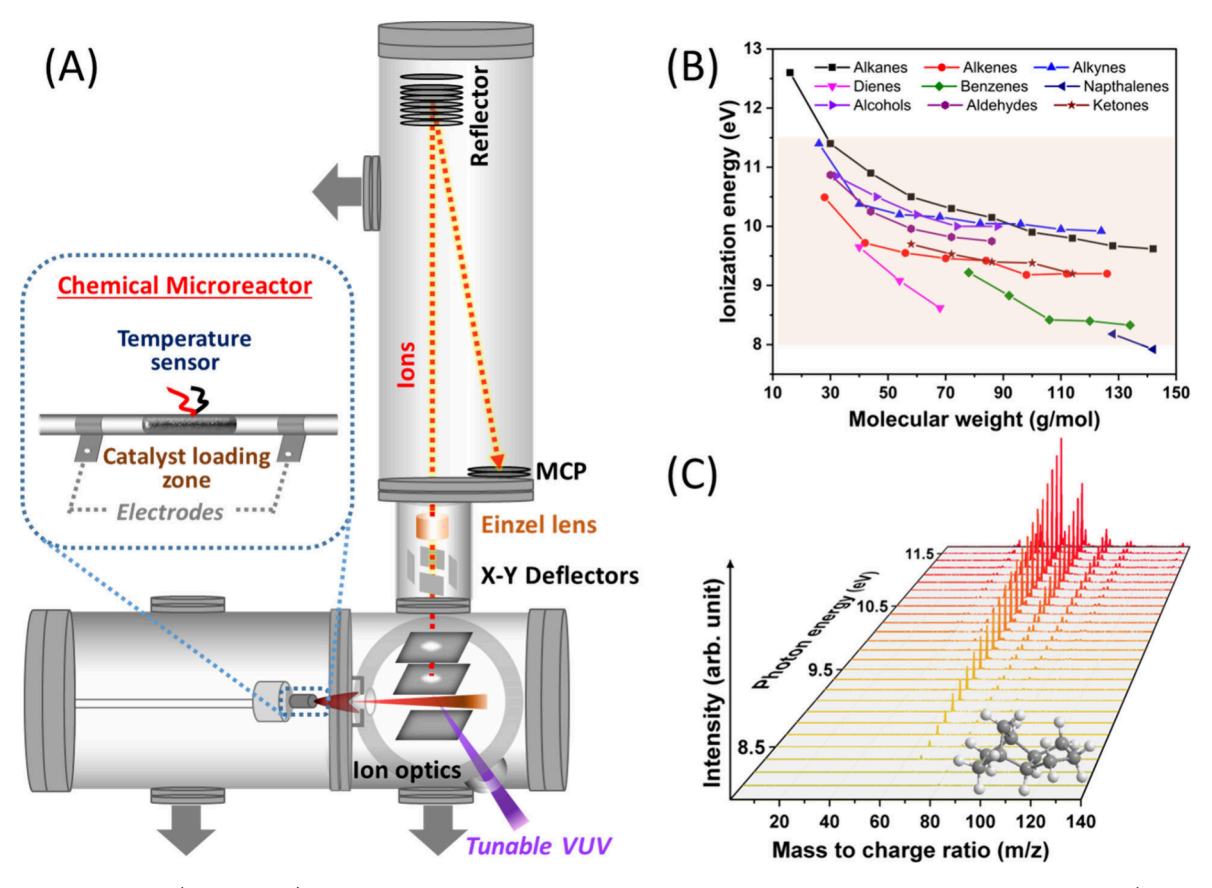
The majority of the operating principles for monitoring and diagnosing combustion processes are based on measuring parameters such as temperature, pressure, flame color imaging,

Received: July 31, 2025
Revised: September 19, 2025
Accepted: September 23, 2025
Published: October 8, 2025





Scheme 1a



"(A) Experimental setup (not to scale) along with the chemical microreactor and tunable vacuum ultraviolet photoionization (VUV-PI) mass spectrometer. The catalyst-loaded microreactor assembly is depicted on the inset of the scheme showing the silicon carbide (SiC) tube, heating electrodes, and a temperature readout sensor. (B) Homologous series of stable hydrocarbon products linked to the oxidative decomposition of common hydrocarbon fuels as a function of ionization energy (IE). The shaded area represents the typical energy scanning range for measuring the photoionization efficiencies (PIEs) of the resulting species. (C) A representative 3D-plot of the acquired mass spectra as a function of photon energy (in eV) to extract PIE curves for the decomposition products formed upon thermocatalytic oxidation of a high energy-density fuel, JP-10 (entrained in 20:80% O₂:He beam) over Ti-Al-B nanopowder.

ignition delay, and combustion product concentration. The widely used laser spark emission spectrometry method, combined with a simple two-component burner that allows for preliminary mixing of gas and air supplied by the compressor, is based on measuring the secondary radiation spectra generated during plasma formation and evolution upon exposing a gas mixture of fuel and oxidizer to strong laser radiation. 14-16 This approach enables both qualitative and quantitative analyses of chemicals, including atomic hydrogen (H), oxygen (O), nitrogen (N), carbon (C), and cyano radicals (CN) throughout the combustion process. Another technique is the acoustically levitated fuel droplet combustion processing system coupled with the time-resolved imaging (optical and thermal) and spectroscopic (FTIR and flame spectroscopy) techniques that are used to determine the ignition delay, ignition temperature, and detection of gas-phase reaction intermediates and products.¹⁷⁻²⁰ This approach accurately measures ignition delays and temperatures. It also detects and quantifies hydrocarbon fuel combustion end products, carbon dioxide (CO₂) and water (H₂O), and identifies key reaction intermediates including hydroxyl (OH), methylidyne (CH), and aluminum monoxide (AlO) during the combustion of AlNP-doped JP-10 nanofuel. 17,18 Most crucially, the identification of lower concentrations of

nascent polyatomic hydrocarbon radicals generated in a complex dynamic process in the presence of fuel additives has been limited by the scope of this technique.

The microflow tube coupled to mass spectrometry, and equipped with either electron impact ionization (EI) or chemical ionization (CI), generally faces a significant challenge in detecting short-lived reaction intermediates.²¹ Additionally, the ionizing source used in the instrument may cause interference by generating additional fragments that have the same mass-to-charge ratio (m/z) as those of the existing products. The development of molecular-beam time-of-flight mass spectrometry (MB-TOF-MS) with a multiphoton ionization technique has enabled the detection of light hydrocarbons, polycyclic aromatic hydrocarbons (PAH), and radicals derived from oxidation and pyrolysis reactions involving combustion but with the limitation of isomer separation. ^{22,23} On the other hand, the shock tube method, when combined with the laser ablation technique, can identify transient radicals like hydroxyl (OH) and methyl (CH₃) along with the stable intermediates, e.g., methane (CH₄), ethylene (C_2H_4) , iso-butene $[CH_2=C(CH_3)_2]$, and aromatics, alongside combustion products like carbon monoxide (CO), carbon dioxide (CO_2) , and water $(H_2O)^{24}$. However, while these experimental approaches are highly appropriate for examining

the pyrolysis and oxidation in liquid fuels, they have limited applicability when it comes to investigating liquid fuels that contain solid additives, thus not forming homogeneous mixtures. ^{25,26}

The heterogeneous catalytic system carrying out reactions at the gas-solid interface has garnered significant interest for enhancing fuel combustion efficiency when solid fuel additives are present. 7,8,10,11 The majority of approaches used to study the catalytic process in heterogeneous systems only imitate the necessary circumstances. Specifically, the batch reactor based pyrolysis-gas chromatography and mass spectrometry (Py-GC/ MS) analysis approach is capable of detecting and quantifying stable products, but these off-line and ex situ detection tools do not have the ability to detect short-lived species.^{27,28} These reactive intermediates (e.g., radicals) formed in the initial stages of the catalysis not only are pivotal to decipher the underlying chemistry but also govern the overall efficiency and performance of the respective catalysts. In addition, a comprehensive inventory of the temperature-dependent products and intermediates is essential to map the thermocatalytic properties of the catalyst as a function of the temperature. For the conventional Py-GC/MS methods, the results vary frequently, necessitating several tests to acquire reliable findings when dealing with nonhomogeneous samples.

On the other hand, laser-vaporized plasmas and pulsed supersonic beams, when combined with mass spectrometric techniques, can only be used to identify the products generated in clusters and gas-phase reactions. ^{29–32} The development of a microreactor with catalyst coating on the tube walls, 33,34 along with photoionization^{35–37} and photoelectron photoion co-incidence detection,³⁴ allows for the isomer-selective detection of gas-phase reactive intermediates (radicals) and stable products. While this technique offers numerous advantages for examining the mechanistic insights of a heterogeneous catalytic system, it is constrained by a low conversion efficiency resulting from inadequate contact time between gaseous reactant molecules and catalyst surfaces. Though the abovementioned analytical approaches detected products generated under heterogeneous catalytic systems, there is a substantial scope for improving the sample preparation and derivatization process to ensure sufficient product concentration for mass spectrometric detection. To circumvent the caveat of exhaustive product detection (stable products and radicals) without large-scale sample preparation and derivatization, we explored a universal catalytic microreactor in a molecular beam that warrants optimal effective interactions between gaseous reactant molecules and catalyst surfaces.

Here, we report a universal catalytic microreactor densely packed with solid catalyst, titanium-aluminum-boron reactive mixed metal nanopowder (Ti-Al-B RMNP) to investigate the thermocatalytic oxidative decomposition of IP-10 utilizing an in situ diagnostics of single photon vacuum ultraviolet (VUV) photoionization mass spectrometry (Scheme 1). This combination of a catalytic microreactor coupled to the molecular beam system of an existing VUV-PI mass spectrometer enables us to intricately study the heterogeneous catalysis at the gassolid interface by detecting and quantifying individual products isomer-selectively. The high energy resolution and tunability of the synchrotron beam allow for the identification of ion signals from isobaric species with adiabatic ionization energies (IE) that lie within 0.2 eV of each other, such as 1,3-pentadiene (IE = 8.6 eV), furan (IE = 8.8 eV), and cyclopentene (IE = 9.0 eV) at m/z = 68. This capability, applied to the measurement of the

isomeric compositions of catalytically generated combustion species, could substantially aid the development of improved kinetic models of combustion and catalytic chemistry.

■ EXPERIMENTAL SECTION

Catalytic Microreactor. The catalytic microreactor is 20 mm long and consists of a 1 mm inner diameter silicon carbide (SiC) tube with heating electrodes and a temperature sensor (Scheme 1A, inset). The heating electrodes are made of molybdenum and are connected to a SiC tube via a thin carbon plate, allowing heat to be transported from the electrodes to the SiC tube. A temperature sensor (type C thermocouple, resistance: 4.3 Ω) is connected in the center of the tube to read out the temperature in the range from 300 to 2000 K. The Ti-Al-B RMNP catalyst fills a short length inside the nozzle and is limited on both sides using glass wool without any hindrance in the movement of components of molecular beam. The microreactor is placed just after the valve connected with a graphite ferrule. The packing length can vary depending on the catalyst type; here, it was set to about 10 mm for the thermocatalytic decomposition of JP-10 in the presence of Ti-Al-B RMNP to prevent molecular mass growths processes that could arise with longer residence times (longer packing length). A direct current (DC) power source is utilized to regulate the temperature of the microreactor with a variance of about ±50 K under present experimental settings.

Single-Photon Tunable Vacuum Ultraviolet Photoionization (VUV-PI) Mass Spectrometer. The singlephoton tunable VUV-PI mass spectrometer has been described previously.³⁸ The gas sample was generated by passing a mixture of helium (He, 99.999% Airgas) and oxygen (O2, 99.99% Airgas) in a volume ratio of 80 to 20% through JP-10 (TCI America; 94%) stored in a stainless-steel bubbler at 298 K. The resulting mixture containing 0.04% of JP-10 was subsequently injected into the catalyst packed reactor, maintaining a temperature range of 300-950 K and a total backing pressure of 500 Torr. After exiting the reactor, the molecular beam containing the thermocatalytically decomposed products was skimmed by a conical skimmer (1 mm in diameter) located 2 cm downstream of the microreactor; the supersonic beam traveled an additional 3 cm to reach the extraction region of the VUV-PI mass spectrometer (Scheme 1A). A quasi-continuous tunable vacuum ultraviolet (VUV) light (beam size: 0.20 mm × 0.01 mm) from the Advanced Light Source's Chemical Dynamics Beamline 9.0.2³⁶ was focused perpendicularly into the molecular beam between the repeller and extractor electrodes within the photon energy range 8 to 16 eV to ionize the individual fragments. Resulting ions were then retrieved by applying a high-voltage pulse of +200 V for 2.5 µs over 1200 V to the repeller electrode. The gate pulse duration was adequate to extract ≥80% of the ions in the interaction zone, thus resulting in sufficient signal intensity. The ions drifted along a field-free region (1 m long) before being reflected by double-stage reflectron plates. Finally, the ions were detected with a time-sensitive chevron microchannel plate (MCP) detector. The mass discrimination was calibrated by recording the ion signals for binary mixtures of propene as a standard (9.7 to 11.75 eV) with nine other target gases: acetylene, ethylene, methanol, propyne, acetaldehyde, ethanol, acetone, benzene, and cyclohexane.³⁹ The achieved mass resolution $(m/\Delta m)$ was up to 400. Oil-free magnetically levitated turbomolecular pumps were used to avoid any background contamination arising from hydrocarbon

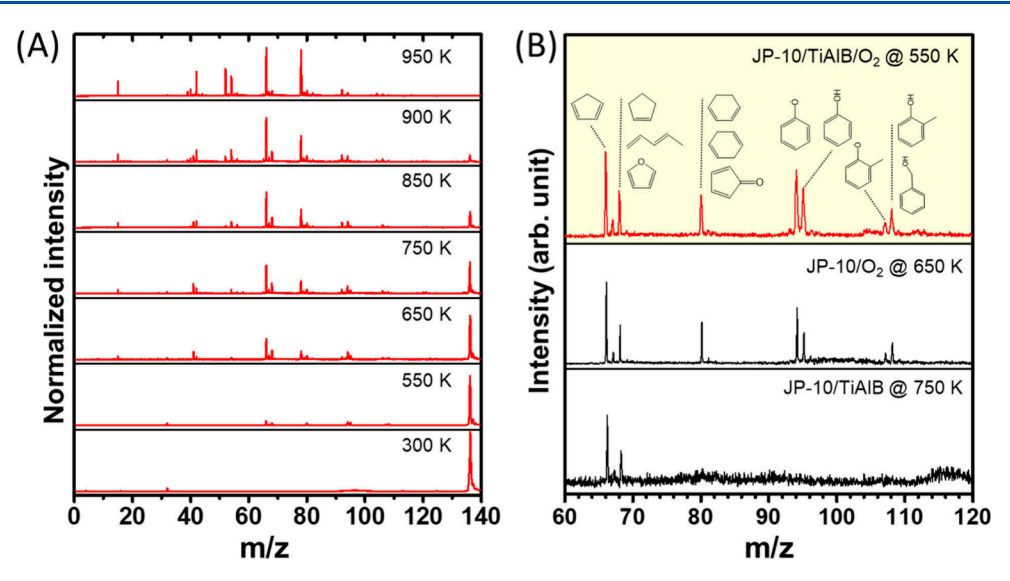


Figure 1. (A) Mass spectra of the products formed upon thermocatalytic oxidative decomposition of JP-10/Ti-Al-B RMNP/O₂ recorded at a photon energy of 10.0 eV in the 300–950 K temperature range. (B) Mass spectra obtained at the initial decomposition temperature under different experimental conditions: JP-10 with Ti-Al-B RMNP (lower panel), JP-10 with O₂ (middle panel), and JP-10 with both Ti-Al-B RMNP and O₂ (top panel). Isomer-selectively identified species at each mass-to-charge ratio (m/z) upon thermal decomposition of JP-10 in the presence of Ti-Al-B RMNP and O₂ are also depicted in the figure (top panel).

oil. The source chamber was maintained at a nominal pressure of 5 \times 10^{-5} Torr during operation by a 2400 L s $^{-1}$ turbomolecular pump. Two turbomolecular pumps of 1000 and 2000 L s $^{-1}$ were used for the main test chamber and the flight tube respectively to achieve pressure as low as 2 \times 10^{-6} Torr. All primary turbomolecular pumps were backed by a 200 L s $^{-1}$ turbomolecular pump to maintain the vacuum system.

Data Acquisition and Extraction Process. The MCP's output signal was collected by a multiscaler (FAST Comtec P7886) with 15008 channels of 2 ns width. The sweep duration of 30 μ s (15008 × 2 ns) was adequate for ions with masses below 200 amu, which have flight durations of less than 25 μ s. The photon energy was calibrated by measuring the photoionization efficiency (PIE) spectra of O₂ in the energy range of 12 to 13 eV. The energy resolution, expressed as the ratio of energy-to-energy width $(E/\Delta E)$, was measured to be 400 with an exit slit width of 200 μ m. A silicon photodiode (International Radiation Detectors, Inc. SXUV-100) measured the current as a function of photon energy, which was then used to normalize the intensity. A 3D plot with three variables, m/z, intensity, and photon energy (in eV), was recorded using home-built LABVIEW software. The PIE spectra were retrieved from the 3D data by using the following strategy. The first step gathered a 2D figure with two variables displayed on the x- and y-axes and a third variable with a set range value. The third variable range decided the energy range that was being sliced off from the original 3D data. Essentially, the "slicing" consists of fixing one variable and plotting the other two. For example, to extract the PIE curve, the intensity versus m/z 2D image in a fixed energy range (8.0–11.5 eV in this case) needs to be obtained first. Then m/z of particular interest is vertically sliced to extract the PIE curves (Scheme 1B,C). All of the processes were carried out using LABVIEW software.

■ RESULTS AND DISCUSSION

Mass Spectra. The JP-10 molecule comprises three fused, strained five-membered ring moieties within a single structure,

exhibiting a high volumetric energy density of 39.6 kJ cm⁻³. Figure 1A depicts typical mass spectra of thermocatalytic oxidative decomposition of JP-10 over Ti-Al-B RMNP catalyst obtained at defined intervals (100 K) from 300 to 950 K at a fixed ionization energy of 10.0 eV. The mass spectrum at 300 K shows only four peaks, the most intense of which is at m/z =136 (parent molecular ion, $C_{10}H_{16}^{+}$) and is nearby the weak ¹³C counterpart at $m/z = 137 (^{13}CC_9H_{16}^+)$ and at m/z = 4 and 32. A trace amount of higher harmonic VUV light photoionizes molecular oxygen (O2) and helium (He), producing peaks at m/z = 32 (weak) and m/z = 4 (very weak), respectively. By systematically raising the temperature of the microreactor and documenting the associated mass spectra, the formation of products was first observed at a temperature as low as 550 K, indicating the commencement of thermocatalytic oxidative decomposition of JP-10. In addition to the mass peaks observed at 300 K, eight additional peaks at m/z = 66, 67, 68, 80, 94, 95, 107, and 108 emerged. The commencement of catalytic oxidation of JP-10 was found to be 100 and 200 K lower than the decomposition of JP-10 in the individual presence of O₂ and Ti-Al-B RMNP (Figure 1B).^{7,40}

As the temperature was raised by 100 K, the number of mass peaks increased along with the pre-existing mass peaks that were seen at the starting decomposition temperature of 550 K. This implies that the products associated with these m/z values observed at 550 K may determine the feasible disintegration pathways of JP-10. Upon further increasing the temperature, the parent JP-10 ion peak disappeared entirely at 950 K, and the most intense mass peaks emerged at m/z = 15, 42, 52, 54,66, and 78. Notably, no signal was seen at m/z values higher than 136 $(C_{10}H_{16}^{+})$ and 137 $(^{13}CC_{9}H_{16}^{+})$ in any spectra recorded at a different temperature, excluding the possibility of molecular mass growth in the context of the current experimental conditions. The mass spectrum solely can elucidate the structure of low molecular weight species up to m/z = 28; however, it is challenging to differentiate isobaric molecules with large molecular weight that contain more than two carbon atoms and requires isomer-selective identification.

Selective identification and quantification of each species (closed-shell molecules and radicals) can be executed with a single-photon tunable VUV-PI mass spectrometer by generating characteristic photoionization efficiency (PIE) curves, discussed later.

Decomposition Profile. The major objectives of the decomposition profile are to provide a better understanding of the thermal stability of the fuel JP-10 in the presence of the catalyst Ti-Al-B RMNP. For quantitative analysis, the decomposition profiles were retrieved using the ratio of decomposed fuel to intact fuel amount calculated from the above-mentioned mass spectra recorded at various temperatures. It implies that the full consumption of fuel represented as unity and zero indicates no reaction.

The area of each individual peak of three measurements was calculated, and the standard deviation was shown as an error bar to ensure the profile reproducibility. Figure 2 depicts the

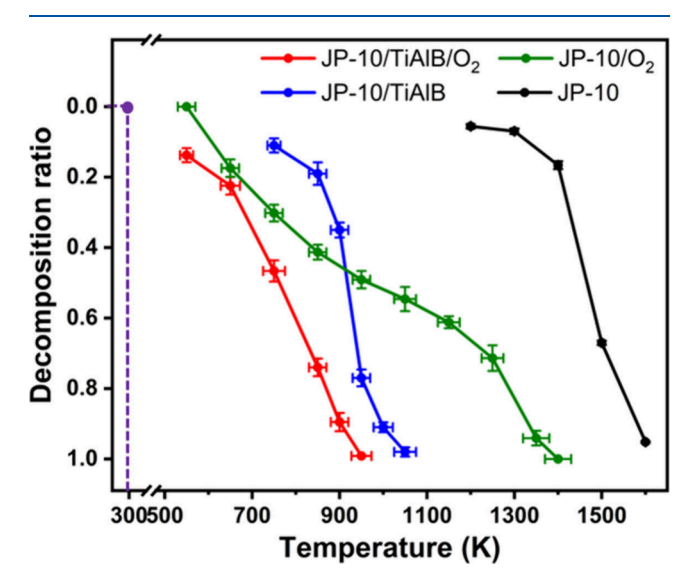


Figure 2. Decomposition ratio profiles for JP-10 passing through the high-temperature chemical microreactor packed with (red and blue traces) and without (olive and black traces) Ti-Al-B RMNP. Oxygen (O_2 , 20%) mixed with helium (He, 80%) is utilized for the oxidation (red and olive traces) process. Efficient decomposition is achieved in the presence of both Ti-Al-B RMNP and O_2 (red trace).

plot of decomposition ratios as a function of temperature for four different sets of reaction conditions: (i) pyrolysis (black trace; carrier gas, helium), (ii) oxidation (green trace; carrier gas, helium-oxygen mixture), (iii) catalytic decomposition (blue trace; catalyst, Ti-Al-B RMNP), and (iv) oxidation in the presence of Ti-Al-B RMNP (red trace; carrier gas, heliumoxygen mixture) of JP-10. The overall pattern for the decomposition ratio curves undergoing thermocatalytic oxidation is remarkably distinct from the normal oxidation of JP-10. The presence of Ti-Al-B RMNP resulted in a significant lowering of the full decomposition temperature for JP-10 by 450 K compared to its oxidation without the catalyst. Critically, the thermal decomposition of JP-10 begins to occur at a significantly higher temperature, specifically at 1200 K, while total decomposition occurs at 1600 K.4 observations suggest that the Ti-Al-B RMNP exhibits significant catalytic activity toward thermal decomposition of the fuel JP-10, thus lowering the full decomposition temperature drastically.

Product Identification and Stability. To investigate the catalytic effect of Ti-Al-B RMNP on JP-10 oxidation, it is important to identify the individual products formed during the thermocatalytic oxidative decomposition process. This was performed by first extracting the photoionization efficiency (PIE) curves at each m/z and fitted with characteristic PIE curves, while for multiple isobaric contributions, linear combinations of the respective reference PIE curves are used. These carefully fitted curves ensure the precise quantification of all products. Altogether 59 products were detected during the thermocatalytic oxidative decomposition of JP-10 in the presence of Ti-Al-B RMNP catalyst at complete decomposition temperature of 950 K. The reaction products can be divided into two groups, (i) oxidized species and (ii) hydrocarbons, which include both closed-shell molecules and radicals.

As the number of peaks increases with temperature, it would be much more straightforward to identify and quantify distinct isomers at each m/z value recorded at the start of the catalytic decomposition process at 550 K. At this temperature, the mass peaks at m/z = 66, 68, 80, 94, 95, 107, and 108 are assigned with various hydrocarbons in the form of 1,3-cyclopentadiene (C_5H_6) , cyclopentene/1,3-pentadiene (C_5H_8) , and 1,3/1,4-cyclohexadiene (C_6H_8) as well as oxidized compounds in the form of furan (C_4H_4O) , 2,4-cyclopentadiene-1-one (C_5H_4O) , phenol (C_6H_5OH) , 1,3-cyclohexadienyloxy radical $(C_6H_7O^{\bullet})$, methylphenoxy radical $(C_7H_7O^{\bullet})$, cresol $(CH_3C_6H_4OH)$, and benzyl alcohol $(C_6H_5CH_2OH)$ (Figure 3A). The mass peak at m/z = 67 corresponding to the ^{13}C counterpart of 1,3-cyclopentadiene $(^{13}CC_4H_6)$ (PIE not shown) is also identified.

In contrast, thermocatalytic decomposition of JP-10 in the presence of Ti-Al-B RMNP at a commencement temperature of 750 K resulted in just two mass peaks at m/z=66 and 68, which correspond to 1,3-cyclopentadiene (C_5H_6) and cyclopentene/1,3-pentadiene (C_5H_8), respectively. The formation of cyclopentadiene (c- C_5H_8 , m/z=66) and cyclopentene (c- C_5H_8 , m/z=68) is attributed to a ring-opening mechanism involving intense C–H activation by Ti-Al-B RMNP followed by sequential C–C bond cleavages and dehydrogenation. It has been found that the catalyst has a significant impact on catalytic activity and selectivity due to its unique structural arrangement of the constituent atoms. Furthermore, cyclopentene (c- C_5H_8) can undergo isomerization to 1,3-pentadiene (C_5H_8) in the gaseous state at the specified temperature.

To rule out the individual influence of oxygen, the product formations at the commencement temperature for oxidative decomposition of JP-10 without a catalyst (650 K) are analyzed as well. The identified product distributions for both JP-10s oxidative decomposition, with and without a catalyst, consistently contain five- and six-membered cyclic hydrocarbons, oxygenated molecules, and radicals. It is worth noting that the commencing temperature for the oxidative decomposition of JP-10 with the Ti-Al-B RMNP catalyst is 100 K lower than that of JP-10 without the catalyst.

Recent electronic structure studies revealed that JP-10 pyrolysis is primarily initiated by C–H bond cleavages, which result in the formation of six distinct JP-10 carbon-centered ($C_{10}H_{15}^{\bullet}$) radicals, followed by strained C–C bond rupture. Anote that the intramolecular hydrogen rearrangement in JP-10 radicals is considerably hampered by their fused ring structure, resulting in each primary hydrogen abstraction reaction launching a distinct decomposition pathway with a distinctive set of products. These reactions are highly

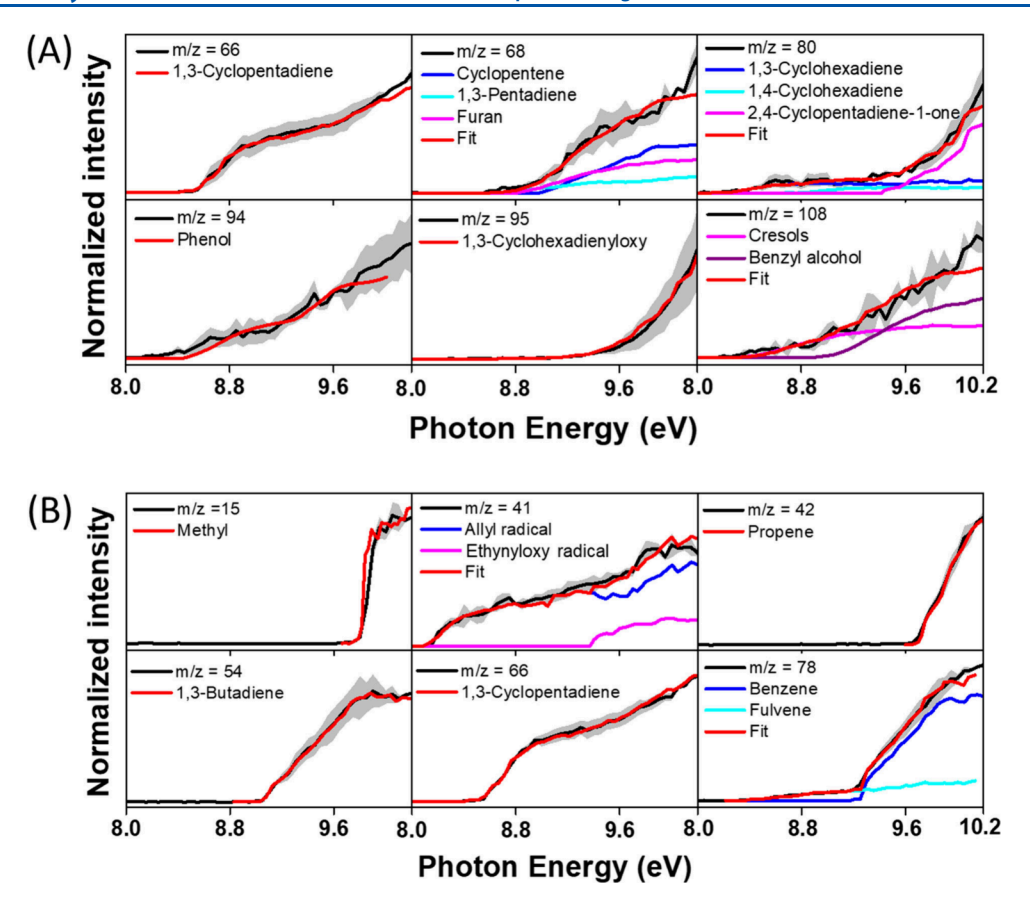


Figure 3. (A) The PIE curves of the listed products that were identified at an initial temperature of 550 K upon thermocatalytic oxidative decomposition of JP-10 by Ti-Al-B RMNP. (B) PIE curves of the dominant products generated at the complete decomposition temperature of 950 K under identical conditions. The color code is as follows: experimental PIE curves (black traces), the isomer-selectively detected hydrocarbons (blue and cyan traces), oxidized (magenta traces) products, and the total fitted curve (red traces).

endoergic, requiring around 400 kJ mol⁻¹, which aligns with the first decomposition temperature of JP-10, 1200 K.⁴¹ In presence of the Ti-Al-B catalyst, the Ti atom exhibits an ideal geometrical compatibility with the structure of JP-10, facilitating the concurrent activation of numerous (3, 4, or even 5) C–H bonds inside a single molecule with a reduced energy barrier of 83 kJ mol⁻¹ - revealed exploiting a model cluster of the mixed nanoparticles based on the comprehensive experimental characterizations.⁴⁰ This decrease in the energy barrier is also reflected in the experimentally recorded temperature at which the decomposition begins, which is 750 K.

Under catalytic oxidation conditions in the presence of the Ti-Al-B RMNP, the commencing decomposition temperature reduces to 550 K. Even this value is lower than that of JP-10 oxidation without any catalyst (650 K). The early onset in the starting decomposition temperature suggests an existence of a more favorable decomposition pathway for JP-10 by further lowering the energy barrier of C-H bond activation. This, for example, may be due to surface bound reactions of JP-10 and molecular oxygen on the Ti-Al-B catalyst, where the Ti-Al-B RMNPs likely bring the reactant molecules, JP-10 and oxygen, closer, resulting in an energetically favorable hydrogen abstraction from JP-10. Eventually, the hot Ti-Al-B RMNP surface can react with molecular oxygen too, producing boron monoxide (BO), aluminum monoxide (AlO), and titanium monoxide (TiO) species, among which BO and AlO represent a highly reactive pool of radicals capable of abstracting atomic

hydrogen from JP-10 through low-energy transition states, with an energy requirement as low as approximately 5 kJ mol $^{-1}$. These result in the formation of $\rm C_{10}H_{15}$ radicals alongside the hydrogen abstraction products boron hydroxide (HBO), aluminum hydroxide (AlOH), and titanium hydroxide (TiOH), respectively. Previous electronic structure theory calculations revealed that TiO-initiated reaction channels are highly endoergic, in the range of 204–248 kJ mol $^{-1}$; thus they cannot compete with energetically favorable BO- and AlO-mediated pathways. As soon as a $\rm C_{10}H_{15}$ radical is formed, the oxidation reactions may proceed further via addition of molecular oxygen to the available radical sites, followed by isomerization and/or fragmentation of reactive, oxygenated intermediates, yielding oxygenated as well as hydrocarbon species. 20

As the temperature increases, the chemical complexity of the products increases. This pattern aligns with our prior findings. 7,10,11,41 At this elevated temperature, the major mass peaks are relatively low molecular weight at m/z=15, 41, 42, 54, 66, and 78 are assigned as methyl radical ($^{\bullet}$ CH₃), allyl radical ($^{\bullet}$ C₃H₅), ethynyloxy radical ($^{\bullet}$ CC), propene ($^{\circ}$ C₃H₆), 1,3 butadiene ($^{\circ}$ C₄H₆), 1,3-cyclopentadiene ($^{\circ}$ C₅H₆), and benzene/fulvene ($^{\circ}$ C₆H₆). Unstable enols which cannot be traced by traditional GC or GC-MS methods, such as ethenol/vinyl alcohol ($^{\circ}$ C₂H₃OH) and propen-2-ol ($^{\circ}$ C₃H₅OH) are also detected at 950 K in this study (Figure S2). Figure 3B shows the PIE curves of the major products produced under otherwise identical experimental conditions at a decomposition

Table 1. Compilation of Products along with the Precursor (JP-10) and Their Ionization Energies (I.E.) Identified in the Thermocatalytic Oxidative Decomposition of JP-10 over the Ti-Al-B RMNP

Mass	Molecular formula	Name	Structure	I.E. (eV)
15	CH ₃	Methyl radical	*CH ₃	9.8
16	CH4	Methane	CH ₄	12.6
18	H ₂ O	Water	H_O_H	12.6
26	C ₂ H ₂	Acetylene	HC≡CH	11.4
28	C ₂ H ₄	Ethylene	CH ₂ =CH ₂	10.5
29	C ₂ H ₅	Ethyl radical	CH ₃ -CH ₂ ·	8.1
	НСО	Formyl radical	H Ċ O	8.1
30	НСНО	Formaldehyde	H—C H	10.9
39	C ₃ H ₃	Propargyl radical	<u> </u>	8.7
40	CII	Allene	=c=	9.7
40	C ₃ H ₄	Methylacetylene	==-	10.4
41	C ₃ H ₅	Allyl radical	/\.	8.1
41	C ₂ HO	Ethynyloxy radical		9.5
42	C ₃ H ₆	Propene		9.7
	C ₂ H ₃ OH	Ethenol (Vinyl alcohol)	O_H	9.3
44	СН3СНО	Acetaldehyde	_c € H	10.2
52	C ₄ H ₄	Vinylacetylene		9.6
54	C ₄ H ₆	1,3-Butadiene		9.1
56	C4H8 -	1-Butene		9.6
		trans-2-Butene		9.1
	C ₂ H ₃ CHO	2-Propenal	C	10.1
	C ₃ H ₆ O	Acetone		9.7
58		Propanal	^ 0	9.9
		Propen-2-ol	OH	8.6
64	C5H4	Ethynylallene	C	9.2
65	C5H5	Cyclopentadienyl radical		8.4
66	C5H6	1,3-Cyclopentadiene		8.5
	C5H8	Cyclopentene		9.2
68		1,3-Pentadiene		8.6
	C ₄ H ₄ O	Furan		8.9
78	С6Н6	Benzene		9.2
		Fulvene		8.4

Table 1. continued

Mass	Molecular formula	Name	Structure	I.E. (eV)
80	C ₆ H ₈	1,3-Cyclohexadiene		8.3
		1,4-Cyclohexadiene		8.8
	C5H4O	2,4-Cyclopentadiene-1-one		9.4
82	C6H10	Cyclohexene		8.9
		2,4-Hexadiene		8.2
	C5H6O	2-Cyclopenten-1-one		9.4
90	C7H6	5-Ethenylidene-1,3-cyclopentadiene		8.3
91	C7H7	Benzyl radical	<u></u>	7.2
92	C7H8	Toluene		8.8
, <u>-</u>		5-Methylene-1,3-cyclohexadiene		7.9
93	C ₆ H ₅ O	Phenoxy radical	<u> </u>	8.6
94	C ₆ H ₆ O	Phenol	ОН	8.5
95	C ₆ H ₇ O	1,3-Cyclohexadienyloxy radical	<u> </u>	9.0
96	C ₆ H ₈ O	2-Cyclohexen-1-one	<u> </u>	9.2
102	C ₈ H ₆	Phenylacetylene		8.8
104	C ₈ H ₈	Styrene		8.4
	C8H10	p-Xylene		8.5
106		1,3,5-Cyclooctatriene		7.9
	C7H6O	Benzaldehyde	O H	9.5
107	С7Н7О	Methylphenoxy radical	•	8.3
100	C7H8O	Cresols	ОН	8.3
108		Benzyl alcohol	ОН	9.0
117	C9H8	Indene		8.3
116		1-Ethynyl-4-methylbenzene		8.5
118	C9H10	Indane		8.5
121	C ₈ H ₉ O	Dimethylphenoxy radical	Ů.	8.3
136	C10H16	JP-10		9.5

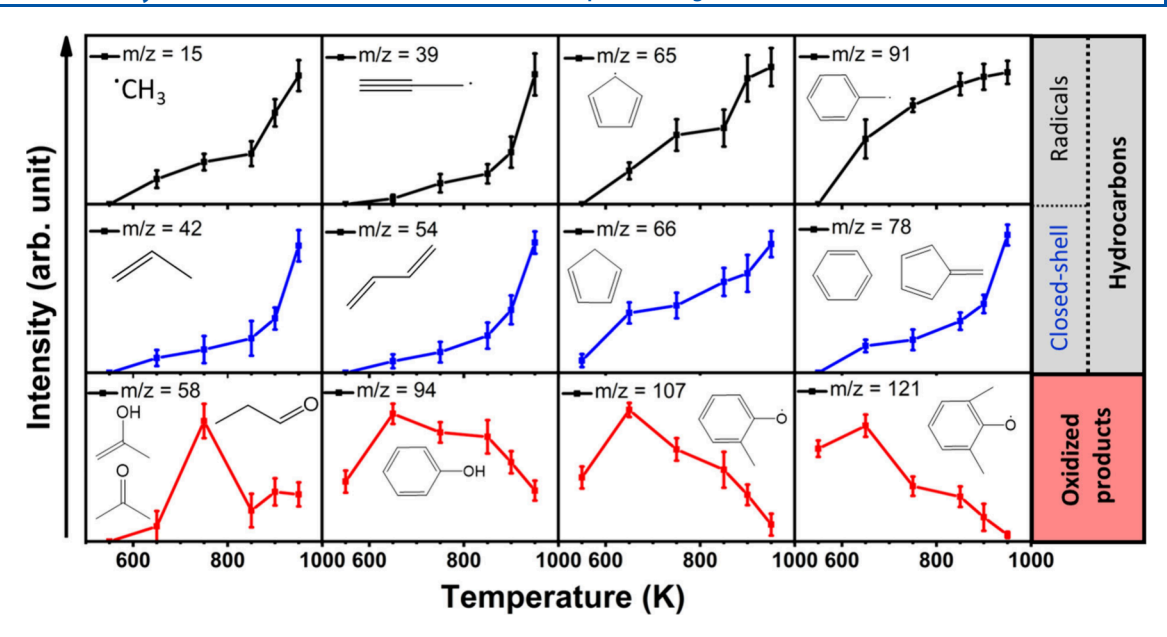


Figure 4. Temperature-dependent relative abundances probed as the respective mass peak intensities for two major types of products: oxygenated and hydrocarbons. The structures of the identified species at the corresponding m/z are also depicted within the panel.

temperature of 950 K. A notable characteristic is the presence of complex radicals and low molecular weight hydrocarbons. This might be due to the extent of thermal energy transfer to the parent molecule exceeding the endoergic (\sim 400 kJ mol⁻¹) pyrolysis pathways of JP-10. The species at m/z=16 (methane, CH₄), 18 (water, H₂O), and 26 (acetylene, C₂H₂) with the ionization energy higher than 11.5 eV were identified from the mass spectra recorded at an energy of 15.4 eV (Figure S1). Figures S2 and S3 show the remaining PIE's for oxidized species and hydrocarbons, respectively. All of the identified species are listed in Table 1.

Figure 4 shows a normalized intensity plot for the major oxygenated and hydrocarbon species detected in this study to evaluate the product formation and stability at different temperatures. The mass peaks at m/z=58, 94, 107, and 121, which correspond to oxidized products, exhibit bell-shaped temperature-dependent yields with maxima observed in the temperature range of 650 ± 100 K. However, the trend in the temperature-dependent abundances of hydrocarbons, which include radicals and closed-shell species, differs greatly from that of the oxidized products and is more favorable at higher temperatures. This suggests that catalytic oxidation and pyrolysis are competing processes at elevated temperatures within the range of 650 to 950 K.

Temperature-Dependent Relative Product Yields. In order to visualize the quantitative product distribution over the entire temperature range, the bar charts of the branching ratios of each product formed during the thermocatalytic oxidative decomposition of JP-10 with Ti-Al-B RMNP are shown at three different temperatures: initial (550 K), intermediate (750 K), and complete decomposition (950 K) temperatures (Figure 5A). The respective individual branching ratios are calculated by accounting for the photoionization cross section, $\sigma_i(E)$, and the mole fraction, $X_i(T)$, of the individual species by the following equations.

$$R_i = \frac{X_i(T)}{\sum X_i(T)} \tag{1}$$

$$X_i(T) \propto \frac{S_i(T, E)}{\sigma_i(E)D_i}$$
 (2)

where $S_i(T,E)$ is the normalized ion intensity, and (D_i) is the mass discrimination factor. The mass discrimination factors were taken from ref 42 and determined to be $(m_i)^{0.51\pm0.11}$. The data obtained at 15.4 eV were used to calculate the branching ratios of methane, water, and acetylene.

At the initial decomposition temperature (550 K) of JP-10 (Figures 5A and S4), the most notable primary products that form are 1,3-cyclopentadiene (C_5H_6 , 27.6 \pm 1.1%), 1,3-cyclohexadienyloxy radical ($C_6H_7O^{\bullet}$, 18.45 \pm 0.75%), phenol (C_6H_5OH , 9.85 \pm 0.80%), and 2,4-cyclopentadiene-1-one (C_5H_4O , 4.8 \pm 0.8%). Other minor products include cyclopentene (C_5H_8), 1,3-pentadiene (C_5H_8), furan (C_4H_4O), the methylphenoxy radical (($C_6H_3C_6H_4O^{\bullet}$), cresols ($C_6H_3C_6H_4OH$), and benzyl alcohol ($C_6H_5CH_2OH$). Almost equal quantities of the hydrocarbon and oxygenated products are generated. All of these are cyclic species with the exception of 1,3-pentadiene (C_5H_8). As the temperature rises, the openchain oxygenated and hydrocarbon species dominate the product spectrum (Figure 5A).

Furthermore, the generation of low molecular weight compounds including hydrocarbons and oxygenated species is more prominent at complete decomposition temperature in the presence of a Ti-Al-B RMNP catalyst (Figure 5B), indicating that at high temperatures, the catalyst Ti-Al-B also facilitates ring disruption of initially formed five- or sixmembered cyclic compounds and radicals. Thus, the critical temperature for the complete oxidative decomposition of JP-10 was reduced from 1400 to 950 K due to an enhanced efficiency of the Ti-Al-B RMNP catalyst.

Isomer selective identification and quantification of thermocatalytic oxidative decomposition products, including stable molecules and short-lived radicals, in each desired temperature range could greatly contribute to the construction of improved kinetic models of combustion chemistry. Although VUV-PI mass spectrometry is an ultrasensitive technique for identifying closed-shell and radical products

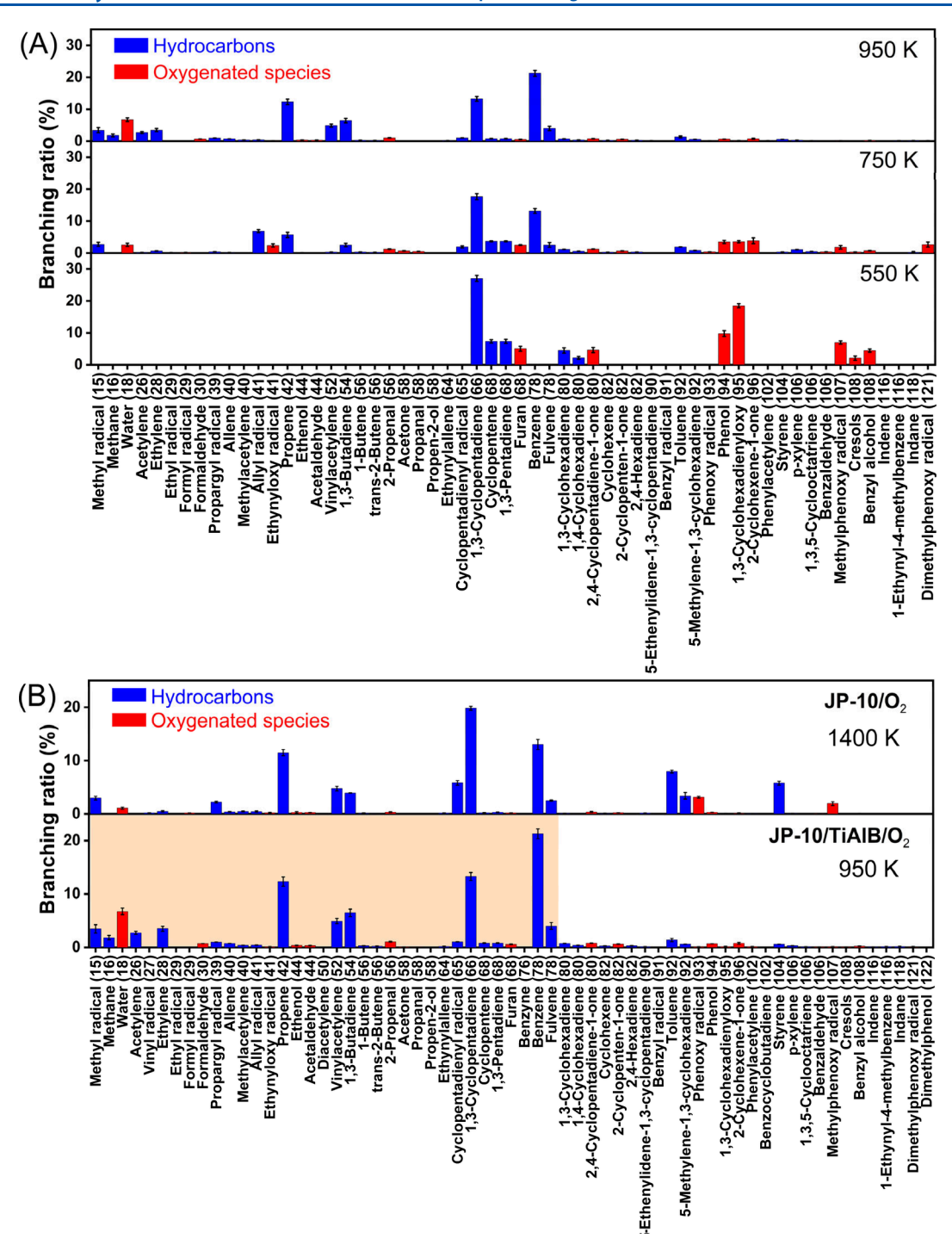


Figure 5. (A) Overall branching ratios of the products evaluated in the thermocatalytic oxidative decomposition of JP-10 by Ti-Al-B RMNP at three distinct temperatures: initial (550 K), intermediate (750 K), and complete decomposition (950 K) temperature. (B) Comparison of the branching ratios for the oxidative decomposition of JP-10 with (bottom panel) and without (top panel) Ti-Al-B RMNP at complete decomposition temperatures of 950 and 1400 K, respectively. The shaded area (bottom panel) represents the efficient formation of lighter hydrocarbons during oxidation.

isomer-selectively, the use of synchrotron light source can be a constraint due to the limited availability and accessibility issues. Alternatively, a VUV light source with an energy resolution of 0.001 eV generated by nonlinear four-wave mixing in a gaseous medium, such as xenon or neon, or a specially designed hollow-core fiber can be used. 43,44

CONCLUSIONS

In summary, we have demonstrated how a chemical microreactor tightly packed with solid nanocatalyst (Ti-Al-B RMNP)-coupled tunable vacuum ultraviolet photoionization (VUV-PI) mass spectrometer can be used to untangle thermocatalytic oxidative decomposition chemistry of high energy-density hydrocarbon fuel JP-10. The approach not only detects and quantifies stable products but also possesses the

capability to identify short-lived closed-shell transient species and radicals central to the decomposition, which cannot be identified by classical analytical techniques involving chromatography. The temperature-dependent product distributions are unambiguously identified by exploiting isomer-selective PIE curves. The primary products consist of cyclic, oxidized species such as 2,4-cyclopentadiene-1-one (C₅H₄O), phenol (C_6H_5OH) , 1,3-cyclohexadienyloxy radical $(C_6H_7O^{\bullet})$, furan (C₄H₄O), cresols (CH₃C₆H₄OH), benzyl alcohol $(C_6H_5CH_2OH)$, and methylphenoxy radical $((CH_3)C_6H_4O^{\bullet})$ along with the five-membered cyclic hydrocarbons, 1,3cyclopentadiene (C₅H₆) and cyclopentene (C₅H₈). Aside from the primary cyclic products, benzene/fulvene (C₆H₆), toluene (C_7H_8) , propene (C_3H_6) , and 1,3-butadiene (C_4H_6) are also detected at elevated temperature (750 K). At the highest temperature (950 K), the generation of low molecular weight compounds including hydrocarbons and oxygenated species is more prominent in the presence of the Ti-Al-B RMNP catalyst, indicating that the catalyst also facilitates ring disruption of the initially formed five- or six-membered cyclic compounds and radicals. The critical temperature for complete oxidative decomposition of JP-10 was lowered by 450 K from 1400 K to 950 K, suggesting an efficient catalytic action of Ti-Al-B RMNP on JP-10 oxidation. Enabling a universal chemical microreactor on VUV-PI mass spectrometer broadens the technique's applicability to study hydrocarbon fuel oxidation and pyrolysis characterization. This makes the technique superior to other conventional analytical techniques such as microflow tube and pyrolysis-gas chromatography coupled with mass spectrometry for investigating hydrocarbon pyrolysis via product detection and quantification.

ASSOCIATED CONTENT

Supporting Information

The Supporting Information is available free of charge at https://pubs.acs.org/doi/10.1021/acs.analchem.5c04691.

Mass spectra of the products formed upon thermocatalytic oxidative decomposition of JP-10 over Ti-Al-B NP recorded at a photon energy of 15.4 eV, photoionization efficiency curves (PIEs) of catalytically decomposed oxidation and hydrocarbon products at 950 K, and branching ratios of the products for oxidative decomposition of JP-10 with and without Ti-Al-B NP at initial temperatures of 550 and 650 K, respectively (PDF)

AUTHOR INFORMATION

Corresponding Authors

Albert Epshteyn — Chemistry Division, U.S. Naval Research Laboratory, Washington D.C. 20375, United States;
orcid.org/0000-0002-4489-2296;

Email: albert.epshteyn@nrl.navy.mil

Musahid Ahmed — Chemical Sciences Division, Lawrence Berkeley National Laboratory, Berkeley, California 94720, United States; orcid.org/0000-0003-1216-673X; Email: mahmed@lbl.gov

Ralf I. Kaiser — Department of Chemistry, University of Hawai'i at Manoa, Honolulu, Hawaii 96822, United States; orcid.org/0000-0002-7233-7206; Email: ralfk@hawaii.edu

Authors

Dababrata Paul — Department of Chemistry, University of Hawai'i at Manoa, Honolulu, Hawaii 96822, United States; orcid.org/0000-0002-5264-3601

Souvick Biswas — Department of Chemistry, University of Hawai'i at Manoa, Honolulu, Hawaii 96822, United States; orcid.org/0000-0002-1643-2663

Nureshan Dias — Chemical Sciences Division, Lawrence Berkeley National Laboratory, Berkeley, California 94720, United States; orcid.org/0000-0002-4518-0901

Matthew T. Finn – Chemistry Division, U.S. Naval Research Laboratory, Washington D.C. 20375, United States

Andrew S. Lipton — Pacific Northwest National Laboratory, Richland, Washington 99354, United States; ocid.org/ 0000-0003-4937-4145

Complete contact information is available at: https://pubs.acs.org/10.1021/acs.analchem.5c04691

Author Contributions

[#]D.P. and S.B. contributed equally.

Notes

The authors declare no competing financial interest.

ACKNOWLEDGMENTS

The Hawaii group was supported by the United States Office of Naval Research (ONR) under Contract N00014-22-1-2010. NRL received support from ONR under Document N0001423WX00734. M.A. and N.D. are supported by the Director, Office of Science, Office of Basic Energy Sciences, of the U.S. Department of Energy under Contract DE-AC02-05CH11231, through the Gas Phase Chemical Physics program of the Chemical Sciences Division. The ALS is supported through the same contract.

REFERENCES

- (1) Chung, H. S.; Chen, C. S. H.; Kremer, R. A.; Boulton, J. R.; Burdette, G. W. *Energy Fuels* **1999**, *13*, 641–649.
- (2) Colket, M. B., III; Spadaccini, L. J. J. Propuls. Power 2001, 17, 315-323.
- (3) Chen, B. H.; Liu, J. Z.; Li, H. P.; Yang, W. J.; Cen, K. F. *J. Therm. Anal. Calorim.* **2019**, *135*, 925–934.
- (4) Li, G.; Hou, B.; Wang, A.; Xin, X.; Cong, Y.; Wang, X.; Li, N.; Zhang, T. Angew. Chem., Int. Ed. 2019, 58, 12154–12158.
- (5) Jin, Y.; Dou, S.; Yang, Q.; Xu, X.; Fu, Q.; Pan, L. Acta Astronaut. **2021**, 185, 70–77.
- (6) Bruno, T. J.; Huber, M. L.; Laesecke, A.; Lemmon, E. W.; Perkins, R. A. Thermochemical and Thermophysical Properties of JP-10. Internal Report NISTIR 6640; NIST, 2006; pp 1–67.
- (7) Biswas, S.; Paul, D.; Dias, N.; Lu, W.; Ahmed, M.; Pantoya, M. L.; Kaiser, R. I. *J. Phys. Chem. A* **2024**, 128, 1665–1684.
- (8) E, X.-T.-F.; Zhang, L.; Wang, F.; Zhang, X.; Zou, J.-J. Front. Chem. Sci. Eng. 2018, 12, 358–366.
- (9) Jin, Y.; Xu, X.; Wang, X.; Dou, S.; Yang, Q.; Pan, L. Proceedings of the Institution of Mechanical Engineers, Part G: J. Aerosp. Eng. 2022, 236, 2580–2591.
- (10) Biswas, S.; Paul, D.; He, C.; Dias, N.; Ahmed, M.; Pantoya, M. L.; Kaiser, R. I. *J. Phys. Chem. Lett.* **2023**, *14*, 9341–9350.
- (11) Biswas, S.; Paul, D.; Dias, N.; Kunzler, K.; Ahmed, M.; Pantoya, M. L.; Kaiser, R. I. *J. Phys. Chem. A* **2024**, *128*, 3613–3624.
- (12) Dinesha, P.; Kumar, S.; Rosen, M. A. Biofuel Res. J. 2021, 8, 1374–1383.
- (13) Paul, D.; Biswas, S.; Yeom, H.; Na, K.; Pantoya, M. L.; Kaiser, R. I. ACS Appl. Mater. Interfaces. **2024**, *16*, 53938–53949.
- (14) Vaganov, M. A.; Kazakov, V. I. J. Phys. Conf. Ser. 2021, 2094, No. 022055.

- (15) Phuoc, T. X.; White, F. P. Fuel 2002, 81, 1761-1765.
- (16) Kazantsev, S. Y.; Kononov, I. G.; Kossyi, I. A.; Tarasova, N. M.; Firsov, K. N. *Plasma Phys. Rep.* **2009**, *35*, 251–257.
- (17) Lucas, M.; Brotton, S. J.; Min, A.; Pantoya, M. L.; Kaiser, R. I. J. Phys. Chem. Lett. **2019**, 10, 5756–5763.
- (18) Lucas, M.; Brotton, S. J.; Min, A.; Woodruff, C.; Pantoya, M. L.; Kaiser, R. I. *J. Phys. Chem. A* **2020**, *124*, 1489–1507.
- (19) Antonov, I.; Chyba, A.; Perera, S. D.; Turner, A. M.; Pantoya, M. L.; Finn, M. T.; Epshteyn, A.; Kaiser, R. I. *J. Phys. Chem. Lett.* **2022**, *13*, 9777–9785.
- (20) Brotton, S. J.; Perera, S. D.; Misra, A.; Kleimeier, N. F.; Turner, A. M.; Kaiser, R. I.; Palenik, M.; Finn, M. T.; Epshteyn, A.; Sun, B. J.; Zhang, L. J.; Chang, A. H. H. J. Phys. Chem. A 2022, 126, 125–144.
- (21) Nakra, S.; Green, R. J.; Anderson, S. L. Combust. Flame 2006, 144, 662-674.
- (22) Apicella, B.; Tregrossi, A.; Oliano, M. M.; Russo, C.; Ciajolo, A. Chemosphere 2021, 276, No. 130174.
- (23) McEnally, C. S.; Pfefferle, L. D.; Atakan, B.; Kohse-Höinghaus, K. Prog. Energy Combust. Sci. 2006, 32, 247–294.
- (24) Gao, C. W.; Vandeputte, A. G.; Yee, N. W.; Green, W. H.; Bonomi, R. E.; Magoon, G. R.; Wong, H.-W.; Oluwole, O. O.; Lewis, D. K.; Vandewiele, N. M.; Van Geem, K. M. Combust. Flame 2015, 162, 3115–3129.
- (25) E, X.-t.-f.; Pan, L.; Zhang, X.; Zou, J.-J. Fuel 2020, 276, No. 118047.
- (26) E, X.-t.-f.; Zhi, X.; Zhang, X.; Wang, L.; Xu, S.; Zou, J.-J. Energy Fuels 2018, 32, 2163–2169.
- (27) Medina-Vera, M. J. Anal. Appl. Pyrolysis 1996, 36, 27-35.
- (28) Picó, Y.; Barceló, D. TrAC, Trends Anal. Chem. 2020, 130, No. 115964.
- (29) Koo, Y.-M.; Kim, J.-H.; Choi, Y.-K.; Lee, H.; Jung, K.-W. J. Phys. Chem. A 2002, 106, 2465–2472.
- (30) Paul, D.; Hong, K.; Kim, T. K.; Jung, K. W. Bull. Korean Chem. Soc. 2010, 31, 271-272.
- (31) Paul, D.; Hong, K.; Kim, T. K.; Oh, J.-S.; Jung, K.-W. Int. J. Mass Spectrom. **2012**, 315, 15–21.
- (32) Paul, D.; Hong, K.; Kim, T. K.; Oh, J.-S.; Jung, K. W. Bull. Korean Chem. Soc. 2012, 33, 1449-1450.
- (33) Hemberger, P.; Custodis, V. B. F.; Bodi, A.; Gerber, T.; van Bokhoven, J. A. *Nat. Commun.* **2017**, *8*, 15946.
- (34) Hemberger, P.; van Bokhoven, J. A.; Pérez-Ramírez, J.; Bodi, A. Catal. Sci. Technol. **2020**, 10, 1975–1990.
- (35) Qi, F. Proc. Combust. Inst. 2013, 34, 33-63.
- (36) Ahmed, M.; Kostko, O. Phys. Chem. Chem. Phys. 2020, 22, 2713-2737.
- (37) Dang, M.; Liu, R.; Dong, F.; Liu, B.; Hou, K. TrAC, Trends Anal. Chem. 2022, 149, No. 116542.
- (38) Nicolas, C.; Shu, J.; Peterka, D. S.; Hochlaf, M.; Poisson, L.; Leone, S. R.; Ahmed, M. J. Am. Chem. Soc. 2006, 128, 220-226.
- (39) Cool, T. A.; McIlroy, A.; Qi, F.; Westmoreland, P. R.; Poisson, L.; Peterka, D. S.; Ahmed, M. Rev. Sci. Instrum. 2005, 76, No. 094102.
- (40) Biswas, S.; Cokas, J.; Gee, W.; Paul, D.; Dias, N.; Morgan, H. W. T.; Finn, M. T.; Hudak, B. M.; Godbold, P. M.; Klug, C. A.; Epshteyn, A.; Alexandrova, A. N.; Ahmed, M.; Kaiser, R. I. *Nat. Commun.* **2025**, *16*, 6793.
- (41) Zhao, L.; Yang, T.; Kaiser, R. I.; Troy, T. P.; Xu, B.; Ahmed, M.; Alarcon, J.; Belisario-Lara, D.; Mebel, A. M.; Zhang, Y.; Cao, C.; Zou, J. Phys. Chem. Chem. Phys. 2017, 19, 15780–15807.
- (42) Urness, K. N.; Guan, Q.; Golan, A.; Daily, J. W.; Nimlos, M. R.; Stanton, J. F.; Ahmed, M.; Ellison, G. B. *J. Chem. Phys.* **2013**, *139*, No. 124305.
- (43) Turner, A. M.; Abplanalp, M. J.; Chen, S. Y.; Chen, Y. T.; Chang, A. H. H.; Kaiser, R. I. *Phys. Chem. Chem. Phys.* **2015**, 17, 27281–27291.
- (44) Forbes, R.; Hockett, P.; Leterrier, Q.; Lausten, R. Opt. Lett. 2024, 49, 3178-3181.

